

Ultrasmall Fe(III)-Tannic Acid Nanoparticles To Prevent Progression of Atherosclerotic Plaques

Dan Mu, Wenshen Wang, Jianhui Li, Pin Lv, Renyuan Liu, Ying Tan, Chongxia Zhong, Yu Qi, Xuan Sun, Yihai Liu, Song Shen, Yuyu Li, Biao Xu,* and Bing Zhang*



Cite This: *ACS Appl. Mater. Interfaces* 2021, 13, 33915–33925



Read Online

ACCESS |



Metrics & More



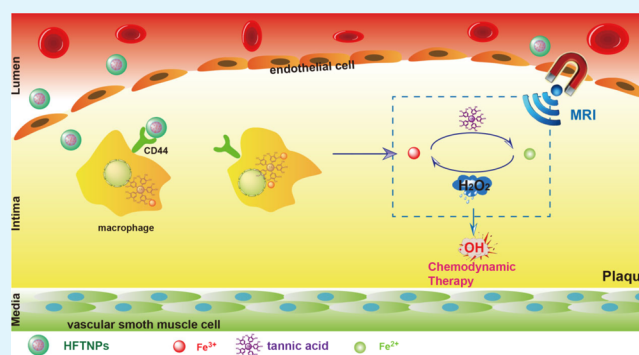
Article Recommendations



Supporting Information

ABSTRACT: Macrophage accumulation is central to the pathogenesis of atherosclerotic plaques. Reducing macrophages in plaques is an appealing approach to attenuate the development of atherosclerosis. Chemodynamic therapy, specifically inhibiting hydrogen peroxide (H_2O_2)-rich cells in slightly acidic micro-environment, has emerged as a new method in tumor treatment. Herein, we manufactured ultrasmall dopamine-modified hyaluronic acid (HD)-stabilized Fe(III)-tannic acid nanoparticles (HFTNPs). HFTNPs can specifically accumulate in inflammatory macrophages in atherosclerotic plaques, provide brighter magnetic resonance images, promote reactive oxygen species (ROS) generation, and induce the death of inflammatory macrophages without damaging normal cells and tissues. In conclusion, HFTNPs have a tremendous potential as safe and effective diagnostic and therapeutic reagents for atherosclerosis.

KEYWORDS: atherosclerosis, chemodynamic therapy, Fe(III)-tannic acid, ultrasmall, magnetic resonance



1. INTRODUCTION

Atherosclerosis has been recognized as a progressive chronic inflammatory disease, featured by the formation of atheromatous plaques in the subendothelial layer of artery wall.^{1–4} A ruptured plaque may induce thrombosis and obstruction in arteries, inducing major clinical consequences.^{5–7} The conventional interventions for preventing the progression of atherosclerotic plaques include life style changes and appropriate medications,^{8–10} such as oral administration of statins or cholesterol absorption inhibitors.^{11–13} In addition, a macrophage-targeted strategy has been recently emerged as a promising solution for specifically attenuating the progression of atherosclerosis.^{14–16}

Biomaterial-based interventions are currently attracting great attention as a promising strategy to facilitate the specific delivery of imaging or therapeutic agents to atherosclerotic plaques.^{17–19} Different types of nanoparticles have been engineered as macrophage-targeted nanomedicine for atherosclerosis therapy.^{20,21} It is reported that cRGD-conjugated nanocarriers based on pluronic polymers have been established to deliver anti-inflammatory interleukin-10 (IL10).²² The IL10-loaded nanocarriers could effectively reverse the production of pro-inflammatory cytokine and ROS by lipopolysaccharide (LPS)-simulated Raw264.7 macrophage cells. In vivo study showed that IL10-loaded nanocarriers successfully reversed the production of pro-inflammatory cytokine by immune cells in atherosclerotic lesion. Another

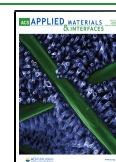
study has also reported a macrophage-derived drug delivery system, combined with membrane vesicles and ROS-responsive nanoparticles, to sequester pro-inflammatory cytokines to suppress local inflammation.²³ It is worth noting that directly inhibiting macrophage proliferation in atherosclerotic plaques has been proved to be a promising strategy.²⁴ All these reports have supported that macrophages are potent and promising target cells for atherosclerosis targeting and therapy.

Chemodynamic therapy (CDT), as a new approach for cancer diagnosis and treatment, works by converting hydrogen peroxide into $\cdot\text{OH}$ via Fenton reaction.²⁵ CDT has been widely explored and different types of nanosystems have been constructed for theranostics.^{26–30} Notably, the conversion efficiency of hydroxyl radicals in CDT nanosystems is sharply restrained in a normal physiological environment: neutral conditions and insufficient H_2O_2 .³¹ The early diagnosis of atherosclerosis is of great importance for the discovery and treatment of cardiovascular disease. Interestingly, iron, as the most critical factor in CDT, is also a very promising contrast

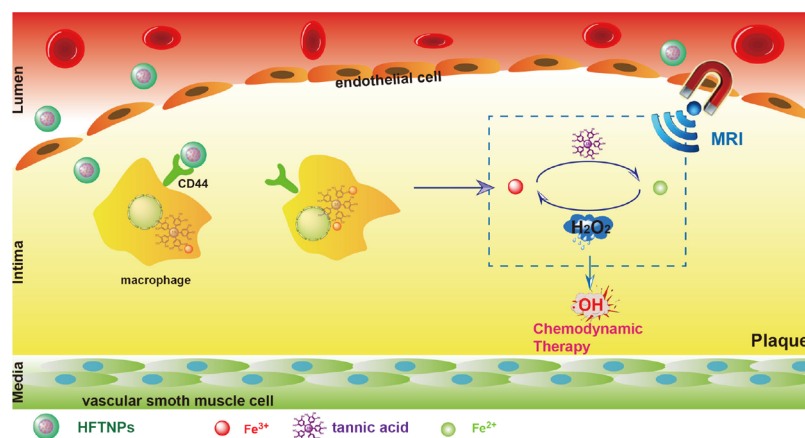
Received: May 24, 2021

Accepted: July 9, 2021

Published: July 19, 2021



Scheme 1. Schematic of Theranostic Applications of HFTNPs in Atherosclerosis



agent of magnetic resonance imaging (MRI).^{32–34} All these data prove that CDT has a tremendous potential in MRI in vivo and inhibition of atherosclerosis progression. However, for all we know, there are currently no reports about CDT relieving or treating atherosclerosis.

Therefore, after absorbing the essence of CDT and considering the microenvironment of atherosclerosis, we designed integrated nanocatalysts targeting macrophages for CDT of atherosclerosis. In our design, the nanocatalysts of Fenton reaction are simply composed of three main components: dopamine-modified hyaluronic acid (HD), ferric ion, and tannic acid (TA). Hyaluronic acid (HA) has been reported to possess high affinity for the macrophage-specific surface receptor CD44.^{35–37} TA, as a FDA-approved food additive, was combined with ferric ions to form a Fe^{3+} -TA complex, where TA worked as iron carriers and also reductant to transfer ferric ions into ferrous ions.^{38,39} HD was conjugated with Fe^{3+} to stabilize the Fe^{3+} -TA complex that is almost insoluble in water.^{40,41} HFTNPs were formed by simply mixing HD, Fe^{3+} , and TA and controlling pH values of coordination. HFTNPs can specifically accumulate in inflammatory macrophages in atherosclerotic plaques, promote ROS generation, and induce the death of inflammatory macrophages via iron-mediated Fenton reaction. In addition, HFTNPs can effectively inhibit the progression of plaques and provide enhanced MRI (Scheme 1). As far as we know, this is the first attempt of using CDT for MRI and attenuation of atherosclerosis.

2. EXPERIMENTAL SECTION

2.1. Materials. HA with the average molecular weight of 10,000 Da and polyvinylpyrrolidone (PVP) were purchased from Shanghai Yuanye Biotechnology (Shanghai, China); Cy5 NHS ester from Shanghai Bide Pharmaceutical Technology (Shanghai, China); TA, Gd-DOTA, adenosine triphosphate (ATP), and LPS from Shanghai McLean Biochemical Technology (Shanghai, China); *N*-hydroxysuccinimide (NHS) and 1-(3-dimethylaminopropyl)-3-ethylcarbodiimide hydrochloride (EDC) from Shanghai Aladdin Biochemical Technology (Shanghai, China); dopamine hydrochloride (Dopa) from Tianjin Xiensi Biochemical Technology (Tianjing, China); 2', 7'-dichlorodihydrofluorescein diacetate (DCF-DA) from Sigma-Aldrich; oxidized low-density lipoprotein (oxLDL) and Dil-oxLDL from Shanghai AngYu Biotechnology Co., Ltd.; and anti-mouse/human CD44-FITC antibody from Shanghai Beyotime Biotechnology (Shanghai, China). Prussian blue iron stain kit was supplied by Yeasen Biotechnology (Shanghai, China). Calcein-AM cell viability assay kit and hydrogen peroxide assay kit were bought from Beyotime

Biotechnology (Nanjing, China). The synthetic procedure of dopamine-modified HA (HD) was described in the [supporting information](#) and its chemical structure was characterized by ^1H NMR as shown in [Figure S1](#).

2.2. Preparation of HFTNPs. HFTNPs were prepared as follows: 5 mg/mL of HD solution was mixed with FeCl_3 to form HD- Fe^{3+} at Dopa: Fe^{3+} molar ratio of 1:0.25 at pH 5.0; TA was added to chelate-conjugated Fe^{3+} to form a HD- Fe^{3+} -TA complex; an excess amount of FeCl_3 was added; and the pH value was raised to 7.4 to produce HFTNPs (Dopa: Fe^{3+} :TA = 1:1:0.25). The final HFTNPs suspension contains 5 mg/mL HD, 1.8 mM Fe^{3+} , and 1.8 mM TA. As a contrast, a different solution or suspension, containing 5 mg/mL PVP or HA, 1.8 mM Fe^{3+} , and 1.8 mM TA, was prepared using the above-mentioned method. HFTNPs with Dopa: Fe^{3+} :TA molar ratio of 1:2:0.5 and 1:4:1 were also prepared using the above-mentioned method.

2.3. Fe(II) Detection. Fe(II) detection was measured according to the literature.³⁹ Briefly, all the samples were suspended in phosphate buffer solution (PBS) containing ATP (1 mg/mL) and reacted with 1, 10-phenanthroline (1 mg/mL) at different times. Then the absorbance was recorded via UV-vis spectrophotometry at 510 nm.

2.4. CD44-Mediated Endocytosis. To visualize the intracellular distribution, HFTNPs were labeled by Cy5 (a red fluorescent dye). Raw264.7 macrophages were seeded in a six-well or a glass-bottom plate. After incubation overnight, HFTNPs (0.5 mg/mL) were added into the plates and cultured with cells for 20 min, 40 min, and 60 min. For visual observation, culture media were removed and macrophages were rinsed with buffer solutions, following fixation using 4% paraformaldehyde and 4', 6-diamidino-2-phenylindole (DAPI) staining. For quantitative analysis, cells were rinsed with buffer solutions, digested with trypsin, and resuspended in PBS.

To investigate CD44-mediated endocytosis, macrophages were seeded in a six-well plate, incubated overnight, and co-cultured with different formulations for 1 h, including PBS, HFTNPs, or HA/HFTNPs (macrophages were preconditioned with 10 mg/mL HA for 60 min). For visual observation, macrophages were rinsed with PBS, following fixation using 4% paraformaldehyde and DAPI staining. Cells were rinsed with PBS and examined via Prussian blue staining method. For quantitative analysis, cells were rinsed with buffer solutions, digested with trypsin, and resuspended in PBS.

2.5. Detection of H_2O_2 and $\cdot\text{OH}$ by DCF-DA. Raw264.7 macrophages were cultured in a six-well plate with 0.1, 0.5, and 1.0 $\mu\text{g/mL}$ LPS for 24 h at 37 °C. Cells treated with PBS were set as control. The concentration of intracellular hydrogen peroxide was performed according to the method of hydrogen peroxide assay kit.

Nonfluorescent DCF-DA can enter the cell and react with ROS to produce fluorescent dichlorofluorescein (DCF) in cells. Raw264.7 and 1.0 $\mu\text{g/mL}$ LPS-activated Raw264.7 macrophages were cultured (density: 3×10^5 cells/well) overnight and incubated with free TA, HD- Fe^{3+} , and HFTNPs for 15, 30, and 60 min, respectively.

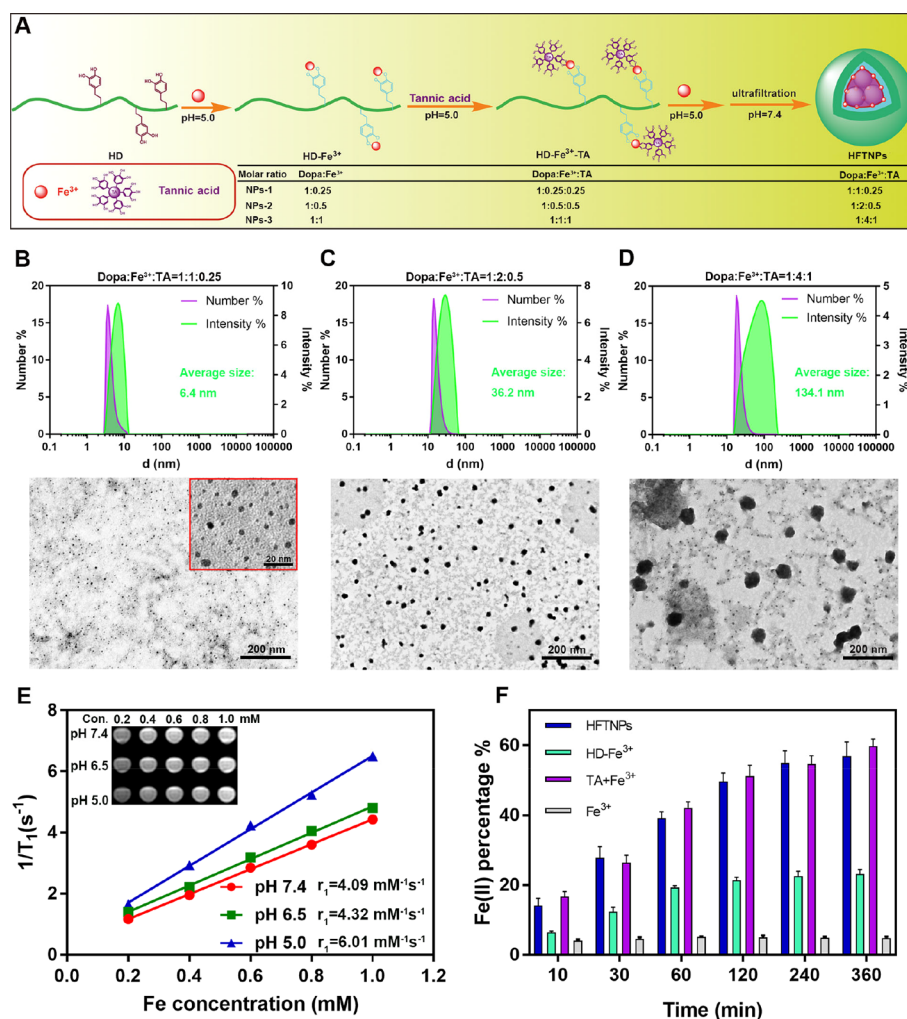


Figure 1. (A) Preparation diagram of HFTNPs. Size distribution and TEM images of HFTNPs with different compositions. (B) Dopa/Fe³⁺/TA = 1:1:0.25; (C) Dopa/Fe³⁺/TA = 1:2:0.5; and (D) Dopa/Fe³⁺/TA = 1:4:1. (E) T₁-weighted images of HFTNPs (Dopa/Fe³⁺/TA = 1:1:0.25) at pH 7.4, 6.5, and 5.0. (F) Detection of Fe(II) in the solution of Fe³⁺, HD-Fe³⁺, TA + Fe³⁺, and HFTNPs.

Raw264.7 macrophages without LPS treatment were used as control. Macrophages were incubated with 10 μ M of DCF-DA for 30 min, following DAPI staining. Cells were washed with PBS for three times and imaged by confocal microscopy. To quantitatively detect intracellular ROS, Raw264.7 and LPS-activated and oxLDL-stimulated Raw264.7 macrophages were treated with different formulations. Cells were incubated with 10 μ M of DCF-DA for 30 min and then evaluated by flow cytometry.

2.6. Cell Viability. The cytotoxicity of Raw264.7 and LPS-activated and oxLDL-stimulated Raw264.7 macrophages was evaluated by MTT assay. Raw264.7 and LPS-activated or oxLDL-stimulated Raw264.7 macrophages were cultured in a 96-well plate (density: 4000 cells/well) overnight and incubated with HD-Fe³⁺ (Fe: 36, 72, 144, 216, 288, and 360 μ M), TA (5.9, 11.8, 23.5, 35.3, 47.0, and 58.8 μ M), and/or HFTNPs (containing TA: 5.9, 11.8, 23.5, 35.3, 47.0, and 58.8 μ M) for 48 h. Cells were treated with 20 μ L of MTT (5 mg/mL) and incubated for 4 h. The medium was replaced with DMSO (200 μ L) to completely dissolve the formazan. The optical density (OD) was recorded by a microplate reader at 490 nm. Cell viability (%) was determined as follows:

$$\text{Cell viability\%} = \frac{\text{OD}_{\text{sample}} - \text{OD}_{\text{blank}}}{\text{OD}_{\text{control}} - \text{OD}_{\text{blank}}} \times 100\% \quad (1)$$

The samples comprised the cells treated with TA, HD-Fe³⁺, and HFTNPs; control comprised the cells treated with DMEM medium; and blank comprised the cells treated with culture medium alone.

2.7. In Vivo Biodistribution. The in vivo distribution of HD-Fe³⁺ and HFTNPs in healthy C57BL/6 mice was evaluated. HD-Fe³⁺ or HFTNPs were injected via tail vein at a dose equivalent to 3 mg/kg of iron. Saline was injected as control. MRI was performed to observe the signal intensity changes in liver, spleen, and kidney. After administration, mice were executed at 2, 4, and 8 h. The organs were carefully collected to analyze iron content by an inductive coupled plasma emission spectrometer (ICP). Tissue sections were also prepared and stained by Prussian blue staining.

2.8. Treatment Protocol. Atherosclerotic apolipoprotein E (ApoE)-deficient mice were randomized into four groups ($n = 5$). The mice were treated with different formulations for 4 weeks. The mice were intravenously injected with TA, HD-Fe³⁺, and HFTNPs at a dose of 15 mg/kg of TA or 2 mg/kg iron every 3 days via tail vein. The mice with saline treatment served as the control. The dosage of iron was chosen according to the literature with some modification.³⁹ The dosing frequency was reduced to minimize the possible side effects.

3. RESULTS AND DISCUSSION

3.1. Fabrication and Characterization of HFTNPs. The fabrication of HFTNPs was described in Figure 1A. First, Fe³⁺ was mixed with HD to form a HD-Fe³⁺ complex at pH 5.0. Fe³⁺ formed a complex with catechol (Dopa) at the molar ratio of 1:1 (mono-complex) at pH 5.0,^{33,42,43} which was supported

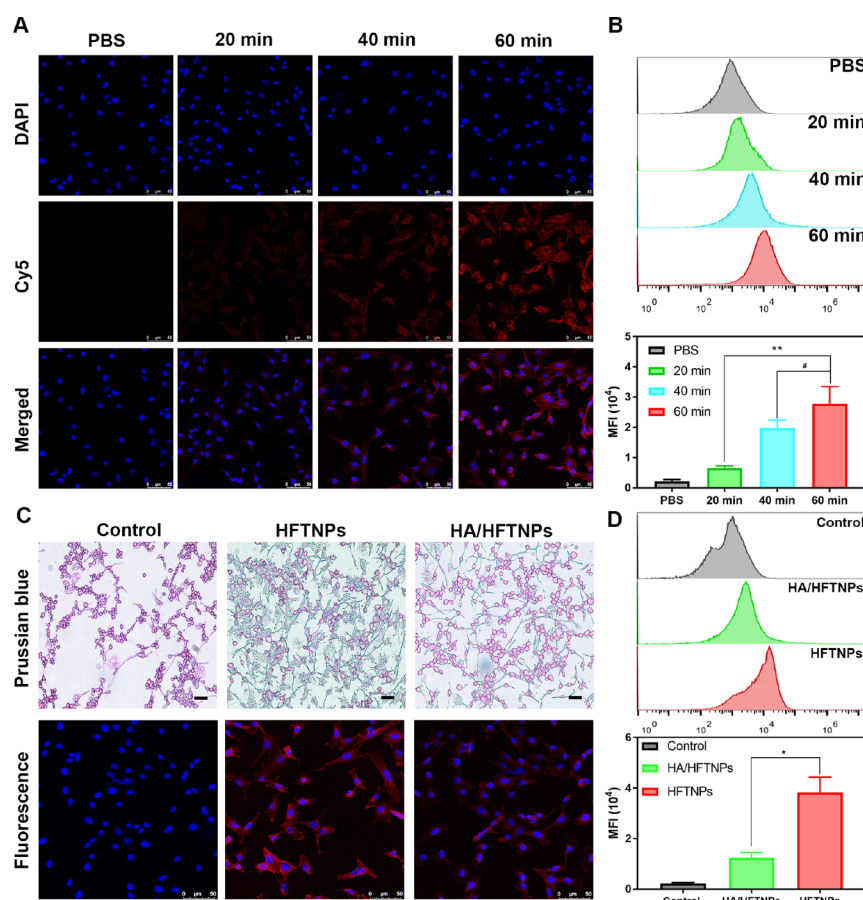


Figure 2. (A) Fluorescent images of Raw264.7 macrophages cultured with Cy5-labeled HFTNPs for 20, 40, and 60 min. Nucleus was labeled using DAPI. Scale bar: 50 μm . (B) Flow cytometry results of Raw264.7 macrophages incubated with Cy5-labeled HFTNPs for 20, 40, and 60 min. (C) Intracellular localization of HFTNPs characterized by Nuclear fast red staining and Prussian blue staining, and fluorescent images of cells pretreated using HA. Scale bar: 50 μm . (D) Flow cytometry analysis of Raw264.7 cells incubated with Cy5-labeled HFTNPs for 60 min with or without HA pretreatment. * $p < 0.05$, ** $p < 0.01$, # $p < 0.05$.

by the characteristic absorption wavelength of mono-complex at ~ 636 nm (Figure S2). Second, TA was added to form a HD- Fe^{3+} -TA complex at the same pH. When $3 < \text{pH} < 6$, Fe^{3+} formed a complex with pyrogallol at the molar ratio of 1:2 (bis-complex),⁴⁴ which indicated that TA can coordinate with HD- Fe^{3+} at pH 5.0. The successful coordination between TA and HD- Fe^{3+} was proved by the characteristic absorption wavelength of bis-complex at ~ 530 nm (Figure S3). At last, additional amount of Fe^{3+} ($\text{Fe}^{3+}:\text{TA} = 3:1$) was added and mixed with HD- Fe^{3+} -TA complex. After raising the pH value to 7.4, redundant Fe^{3+} was removed by ultrafiltration to obtain HFTNPs. In HFTNPs, tris-complex between Fe^{3+} and pyrogallol was formed with the molar ratio of 1:3, which was proved by the characteristic absorption wavelength of tris-complex at ~ 513 nm (Figure S3). The formation of HFTNPs was driven mainly by the coordination between Fe^{3+} and TA. Both Fe^{3+} and TA have good solubility in water, but in situ formed Fe^{3+} -TA complex exhibits poor solubility in water (Figure S4).⁴⁰ Therefore, after additional Fe^{3+} was mixed with HD- Fe^{3+} -TA, the amphiphilic structure was formed between HD and Fe^{3+} -TA complex. Moreover, pyrogallol in HD- Fe^{3+} -TA was connected by Fe^{3+} , leading to the cross-linkage of HFTNPs.

Three types of HFTNPs were prepared with the Dopa: Fe^{3+} :TA molar ratio of 1:1:0.25, 1:2:0.5, and 1:4:1, respectively. The size distribution and morphology of the three

types of HFTNPs were exhibited in Figure 1B, C, and D, respectively. As TA increased, the average diameter of HFTNPs increased gradually. HFTNPs with the Dopa: Fe^{3+} :TA molar ratio of 1:1:0.25 exhibited ultrasmall uniform nanoparticles with the average size of 6.4 nm. HFTNPs with the Dopa: Fe^{3+} :TA molar ratio of 1:2:0.5 also exhibited uniform nanoparticles with the average size of 36.2 nm. The particle size of these two types of HFTNPs measured by DLS was larger than those from TEM photos, which possibly resulted from the particle shrinkage during the preparation of TEM samples. Notably, both large and small nanoparticles can be observed in HFTNPs with the Dopa: Fe^{3+} :TA molar ratio of 1:4:1. This result may be due to the fact that some of Fe^{3+} -TA cannot be fully stabilized by HD, resulting in the formation of larger nanoprecipitates. In view of the ultrasmall and uniform particle size, HFTNPs with the Dopa: Fe^{3+} :TA molar ratio of 1:1:0.25 were used in the subsequent experiments.

Different from normal tissues with pH around 7.4, atherosclerotic lesions are slightly acidic (pH 6.0–6.8) and the pH value in lysosomes of macrophages is much lower than 5.0.¹⁶ Therefore, it is necessary to survey the pH-dependent MR contrast ability of HFTNPs. The longitudinal relaxivity (r_1) of HFTNPs was measured at 7.4, 6.5, and 5.0. As shown in Figure 1E, HFTNPs presented pH-sensitive MRI T_1 -weighted relaxivity. At pH 5.0, the r_1 value of HFTNPs was 1.47-fold higher than that at pH 7.4 and 1.39-fold higher than that at pH

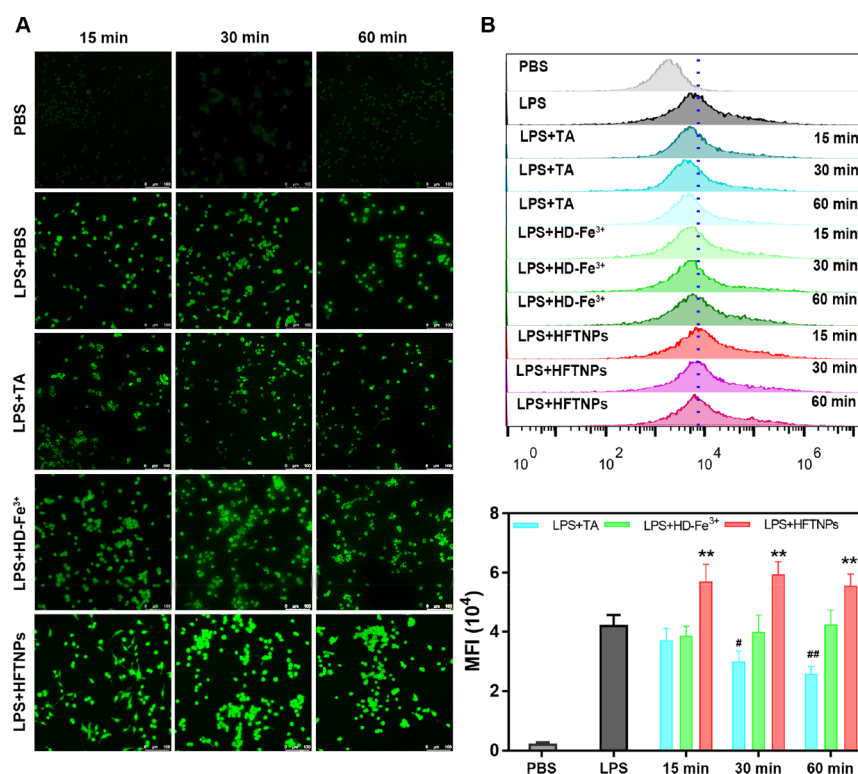


Figure 3. (A) Representative fluorescent images of LPS-activated Raw264.7 macrophages incubated with TA, HD-Fe³⁺, and HFTNPs for 15, 30, and 60 min, respectively. Raw264.7 macrophages were treated with PBS as control. TA: 29.4 μ M, iron: 117.6 μ M. Scale bars: 100 nm. (B) Quantitative analysis of LPS-activated Raw264.7 cells incubated with PBS, TA, HD-Fe³⁺, and HFTNPs for 15, 30, and 60 min by flow cytometry. LPS + HFTNPs vs LPS: ** p < 0.01; LPS + TA vs LPS: # p < 0.05 and ## p < 0.01.

6.5. Notably, r_1 values of HFTNPs at all three pH values were higher than those of Gd-DOTA (contrast agent for clinical use) (Figure S5), indicating excellent MR contrast ability of HFTNPs.

Fe³⁺ could be transformed into Fe²⁺ by polyphenols,³⁹ which helps to increase the catalytic efficiency of Fenton reaction. HFTNPs were dispersed in the solution in the presence of ATP to release Fe³⁺ and TA. The concentration of Fe²⁺ was measured at different time points. As shown in Figure 1F, 49.6% of Fe³⁺ in HFTNPs was reduced within 2 h, and the concentration of Fe²⁺ indistinctively increased in the next 4 h. However, only 23.1% of Fe³⁺ in HD-Fe³⁺ was reduced to Fe²⁺ within 6 h. As a comparison, no significant increase of Fe²⁺ was observed in the Fe³⁺ solution. The results confirmed that Fe³⁺ could be effectively converted into Fe²⁺ by TA in aqueous phase.

3.2. Cellular Uptake. CD44 expression on macrophage cells was measured by CLSM and flow cytometry before and after LPS activation. As shown in Figures S6 and S7, CD44 expression increased by only 13.1% after LPS induction. To study the intracellular internalization of HFTNPs, Raw264.7 macrophages were co-cultured with Cy5-labeled HFTNPs for 20, 40, and 60 min. Figure 2A showed the counterstained nuclei by DAPI. With the increase in incubation time, we observed the continuous increase of red fluorescence signal in cells, which indicates the time-dependent internalization of HFTNPs by cells. Quantitative flow cytometry further confirmed the increased intracellular internalization (Figure 2B). The mean fluorescence signal intensity of cells which were incubated for 60 min was 1.41-fold and 4.29-fold higher than that for 40 and 20 min. To further evaluate CD44-mediated

endocytosis, Raw264.7 macrophages were pretreated with HA for 60 min to partially block CD44 and then incubated with HFTNPs for another 60 min. Nuclear fast red staining was used to reveal cells, and then iron staining was carried out using Prussian blue staining reagent, interacting with Fe³⁺ to produce a blue color. As shown in Figure 2C, Prussian blue staining of cells showed the presence of HFTNPs in Raw264.7 cells. HA pretreatment decreased the internalization of HFTNPs, which is consistent with the fluorescent images of cells. The quantitative results of flow cytometry in Figure 2D showed that the fluorescent signal intensity of cells decreased by 67.3% after HA pretreatment, which indicates the CD44-dependent uptake of HFTNPs.

3.3. •OH Generation. Studies confirmed that iron-based nanocatalysts can markedly elevate the amount of hydroxyl radical (•OH) in some tumor cells.^{45,46} However, whether Fenton reaction catalysts could induce production of •OH in macrophages has not been investigated. LPS is widely used to stimulate Raw264.7 cells into inflammatory macrophages that produce more ROS. Nevertheless, the generation of •OH was dependent on intracellular concentration of hydrogen peroxide (H₂O₂), and it has not been determined against LPS-activated or nonactivated Raw264.7 cells. Hydrogen peroxide assay kit was used to determine the intracellular H₂O₂ (Figure S8). As a result, LPS (0.1, 0.5, and 1.0 μ g/mL) can significantly promote the generation of H₂O₂ in Raw264.7 cells (Figure S9). In particular, the intracellular concentration of H₂O₂ simulated by 1.0 μ g/mL LPS was 2.14-fold higher than that with no LPS.

The production of •OH was tested using a DCF-DA probe. Raw264.7 cells with 1.0 μ g/mL LPS treatment were co-cultured with TA, HD-Fe³⁺, and HFTNPs for 15, 30, and 60

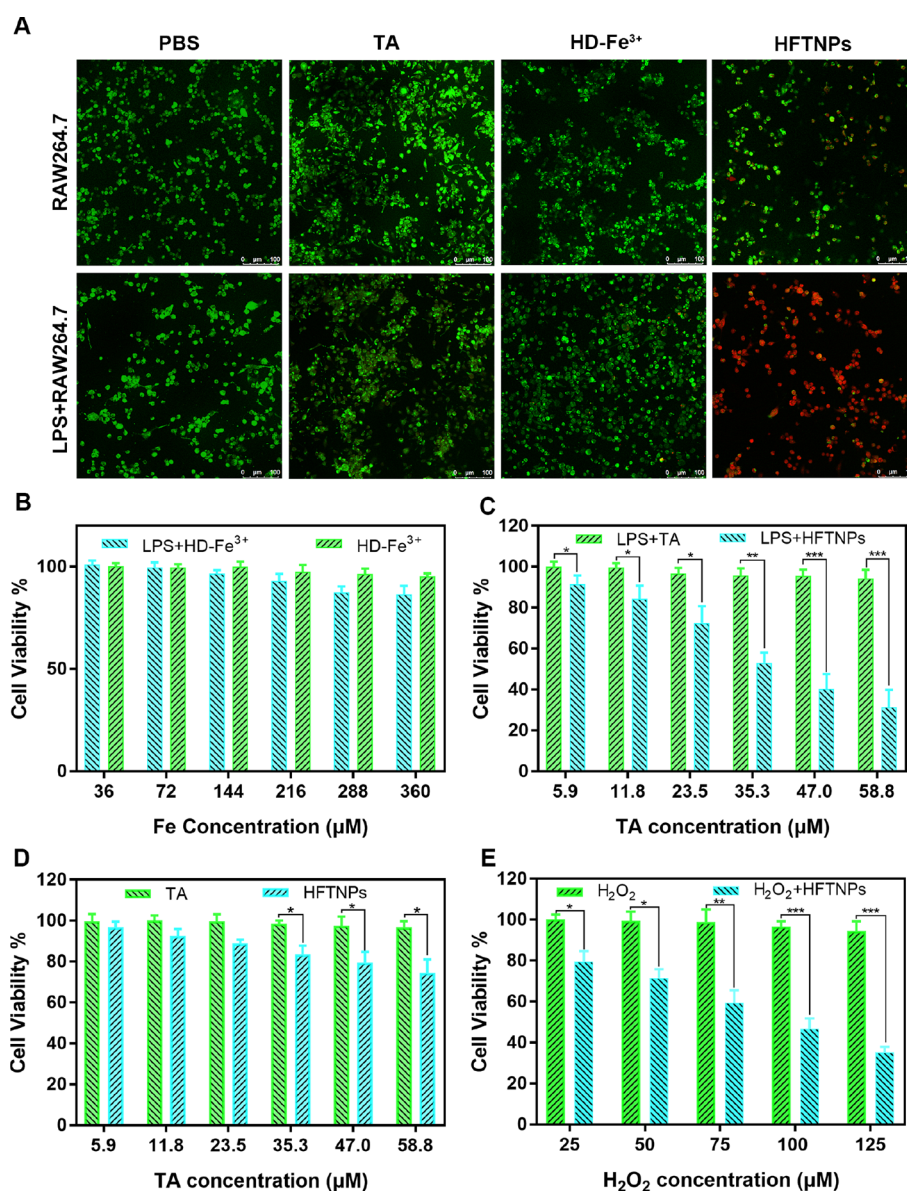


Figure 4. (A) CLSM images of viable or dead cells after PBS, TA, HD-Fe³⁺, and HFTNPs treatment. TA: 29.4 μM or iron: 117.6 μM. Scale bars: 100 nm. (B) Cytotoxicity of HD-Fe³⁺-treated Raw264.7 macrophages with or without LPS activation. Cytotoxicity of LPS-activated Raw264.7 (C) and Raw264.7 macrophages (D) after TA and HFTNPs treatment. (E) Cytotoxicity of Raw264.7 pretreated with different concentrations of H₂O₂ and then treated with HFTNPs (TA: 29.4 μM; Fe: 117.6 μM). **p* < 0.05, ***p* < 0.01, ****p* < 0.001.

min, respectively. Intracellular ROS production was measured as shown in Figure 3A,B, and the intracellular ROS increased dramatically after LPS stimulation. With the extension of culture time, TA showed the ability to reduce ROS, which may be due to its own antioxidant activity. HD-Fe³⁺ did not significantly change the generation of intracellular ROS, which possibly resulted from low conversion of Fe³⁺ to Fe²⁺. Interestingly, HFTNPs further increased the generation of intracellular ROS when prolonging the culture time. The ability of ROS produced by HFTNPs is much stronger than that of HD-Fe³⁺, which is due to the fact that TA can effectively reduce Fe³⁺ to Fe²⁺.³⁹ Thus, the amount of Fe²⁺ in HFTNPs is actually higher than that of HD-Fe³⁺, which is beneficial to maintain the Fenton reaction. Interestingly, the production of ROS decreased slightly after cells were treated with HFTNPs for 60 min, which is probably because the

hydroxyl radicals generated by the Fenton reaction may have induced cell death.

3.4. Cytotoxicity. Raw264.7 macrophages with or without LPS activation were incubated with TA, HD-Fe³⁺, and HFTNPs for 24 h. Calcein-AM and PI were used to detect viable and dead cells. Very few dead macrophages were seen when cells were treated with TA and HD-Fe³⁺ (Figure 4A). A small number of dead Raw264.7 cells were seen when they were treated with HFTNPs. However, a large number of dead LPS-activated Raw264.7 cells were observed when they were treated with HFTNPs, which is consistent with the results as shown in Figure 3. To further explore the cytotoxicity of HFTNPs, the viabilities of cells were assessed by MTT assay. No significant cytotoxicity of HD-Fe³⁺ on Raw264.7 cells was observed (Figure 4B), which was together decided by relatively low concentration of H₂O₂ in Raw264.7 cells and low conversion of Fe³⁺ to Fe²⁺, whereas HD-Fe³⁺ exhibited

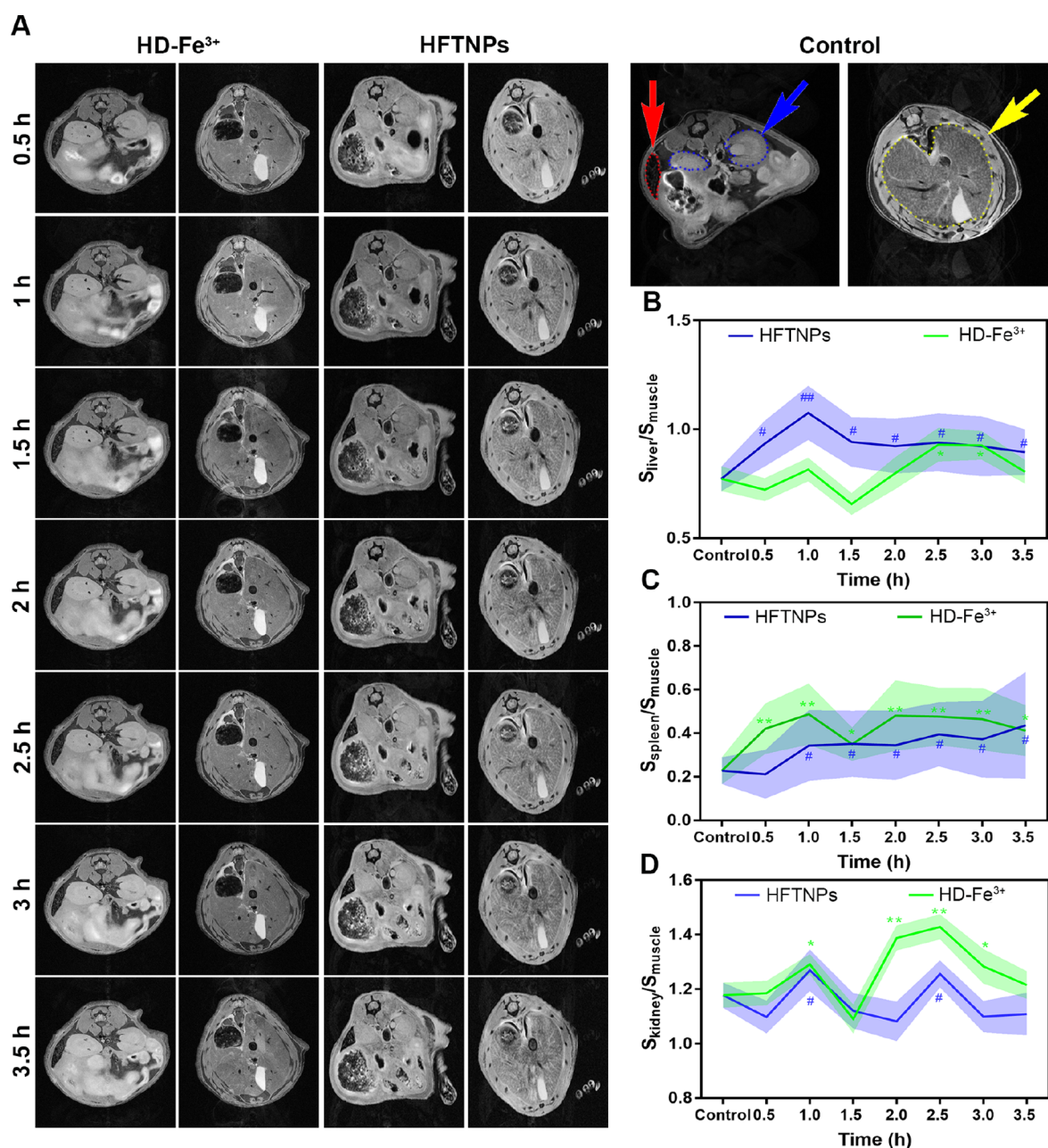


Figure 5. T_1 -weighted MRI images of spleen, kidney, and liver in healthy C57BL/6 mice after injection of HD-Fe³⁺ and HFTNPs. Red line: spleen; blue line: kidney; yellow line: liver. (A) Time-dependent signal-to-noise ratio (SNR) of HD-Fe³⁺ and HFTNPs in liver (B), spleen (C), and kidney (D). HD-Fe³⁺ vs Control: * p < 0.05, ** p < 0.01, and *** p < 0.001; HFTNPs vs Control: # p < 0.05, ## p < 0.01, and ### p < 0.001.

cytotoxicity against LPS-activated Raw264.7 cells with 86.4% of the viability at the maximum test concentration. Figures 4C,D show that TA has no significant cytotoxicity effect on both Raw264.7 and LPS-activated Raw264.7 macrophages. HFTNPs exhibited almost no cytotoxicity on Raw264.7 macrophages, but showed dose-dependent cytotoxicity on LPS-activated Raw264.7 macrophages. When Raw264.7 macrophages were incubated with diverse levels of H₂O₂ and then treated with HFTNPs, cell viability decreased dramatically (Figure 4E), indicating H₂O₂-dependent cytotoxicity of HFTNPs. It is worth noting that HFTNPs exhibited darker purple than HD-Fe³⁺ (caused by the formation of Fe³⁺-TA complex), which would slightly raise the OD values of formazan solution (purple).

To further investigate the effect of HFTNPs, foam cells were induced by oxLDL. The successful induction of foam cells was proved by internalization of oxLDL into macrophages, as shown in Figure S10A and S10B. Notably, oxLDL did not promote the expression of CD44 (Figure S10C), but it did increase the generation of ROS in Raw264.7 macrophages. As depicted in Figure S10D, HFTNPs treatment can also further increase the ROS generation in oxLDL-stimulated Raw264.7 macrophages and thus result in dose-dependent cytotoxicity (Figure S10E).

3.5. In Vivo Distribution. MRI was performed to investigate the distribution of HD-Fe³⁺ and HFTNPs in healthy mice. Within 3.5 h, the MRI signals in liver, kidney, and spleen were measured as shown in Figure 5. HFTNPs showed significant accumulation in liver and spleen, and HD-

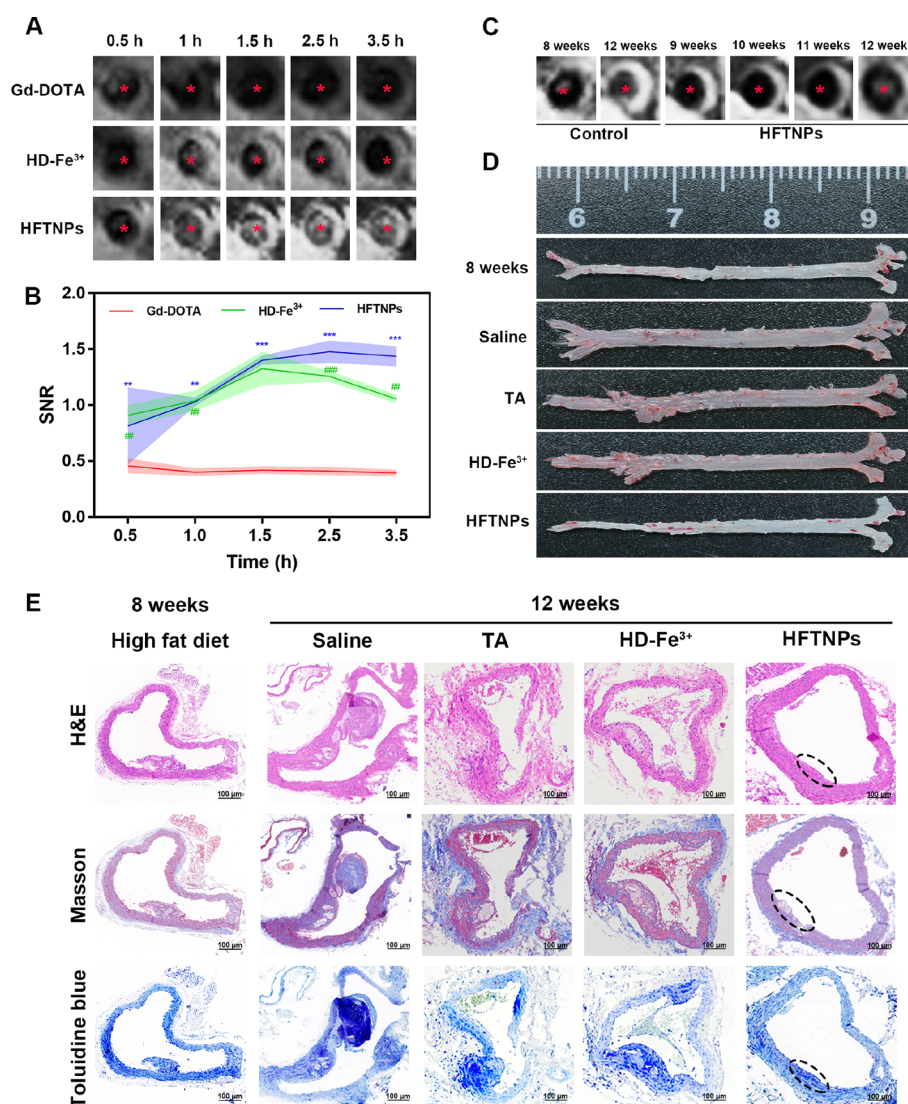


Figure 6. (A) Time-course T₁-weighted MRI images of plaques from ApoE^{-/-} mice after injection of Gd-DOTA, HD-Fe³⁺, and HFTNPs. (B) Time-dependent SNR of Gd-DOTA, HD-Fe³⁺, and HFTNPs. HFTNPs vs Gd-DOTA: **p < 0.01 and ***p < 0.001; HD-Fe³⁺ vs Gd-DOTA: ##p < 0.01 and ###p < 0.001. (C) Typical T₁-weighted MR images of plaques of mice after treated with HFTNPs. (D) Images of ORO-stained aortas from ApoE^{-/-} mice. (E) Representative photographs of plaques stained by H&E, Masson's trichrome, and Toluidine blue. Scale bar: 100 μm.

Fe³⁺ was mainly accumulated in spleen and kidney. This result indicated different excretion pathways of HD-Fe³⁺ and HFTNPs, which probably resulted from different modalities of HD-Fe³⁺ (similar to biomacromolecules) and HFTNPs (nanoparticles). Both HD-Fe³⁺ and HFTNPs showed enhanced MRI signals in the spleen, which may be due to the abundance of macrophages in the spleen that take in HD-Fe³⁺ and HFTNPs. To quantitatively confirm the in vivo distribution of HD-Fe³⁺ and HFTNPs, mice were administered with HD-Fe³⁺ and HFTNPs and killed to collect major organs to measure the iron content at different time points (Figure S11). Elevated iron content was confirmed in spleen within 8 h, whereas other organs exhibited no evident increase of iron. This result can also be observed in the Prussian blue staining images of the tissue sections (Figure S12). After administration for 2 h, the iron concentration in the spleen increased by 459% for HD-Fe³⁺ and 482% for HFTNPs compared with the control group. After 4 h, iron increased by 317% for HD-Fe³⁺ and 206% for HFTNPs. However, after 8 h, HFTNPs could still be detected in the spleen and the iron

concentration increased by 261%, whereas HD-Fe³⁺ could be barely detected. These results suggested that HFTNPs has the potential for longer blood circulation, which warrants adequate targeting of atherosclerotic plaques.

3.6. In Vivo Efficacy of HFTNPs. The MRI contrast-enhancing effect of HFTNPs was investigated in atherosclerotic ApoE^{-/-} mice. The MRI signal intensities of plaques and muscles were measured, and their ratio was used as signal-to-noise ratio (SNR). As shown in Figure 6A and B, both HD-Fe³⁺ and HFTNPs showed higher hyperintense signals in T₁-weighted images than those in Gd-DOTA, indicating successful CD44-mediated plaque targeting. The SNR of HFTNPs was higher than that of HD-Fe³⁺ at 1 h. Furthermore, HFTNPs showed more persistent contrast enhancement within 3.5 h, whereas the MRI contrast-enhancing effect of HD-Fe³⁺ started to decrease in plaque at 1.5 h.

To explore the anti-atherosclerosis potential of HFTNPs, atherosclerotic ApoE^{-/-} mice were randomly grouped into four teams (n = 5) followed by the treatment of TA, HD-Fe³⁺, and HFTNPs via tail veins for 4 weeks. Saline treatment was

used as controls. As shown in Figure 6C, atherosclerotic plaques can be observed clearly after a high-fat diet for 8 weeks. The plaques continued to progress after saline treatment for another 4 weeks (total 12 weeks). After administration of HFTNPs for 4 weeks, plaques can still be observed clearly. Notably, the progression of plaques was inhibited after the treatment of HFTNPs since the 9th week. In addition, the lesion area ratio of plaques was extraordinarily reduced to 9.1% according to Oil Red O (ORO) staining results compared with saline (20.7%), TA (18.4%), and HD-Fe³⁺ (17.9%) treatment (Figures 6D and S13). These results suggested mild inhibition for the progression of plaques. The accumulation of HD-Fe³⁺ and HFTNPs in major organs was investigated by Prussian blue staining. As shown in Figure S14, both HD-Fe³⁺ and HFTNPs can be detected in spleen, and HFTNPs can also be detected in liver, which is consistent with in vivo distribution as depicted in Figure 5.

Immunohistochemistry analysis was used to survey the compositions of atherosclerotic plaques. H&E and Toluidine blue staining showed larger plaques and necrotic core after mice were treated with saline for 4 weeks, indicating continuous progression of the plaques (Figure 6E). Compared with the treatment of TA and HD-Fe³⁺, HFTNPs significantly prevented the progression of plaques and the formation of necrotic cores, but the plaques were still observed (the dotted circle). In addition, Masson staining results showed that HFTNPs can also effectively reduce the production of collagen. At last, biosafety is essential for diagnostic and therapeutic reagents. Therefore, adverse effects were studied by H&E staining after treatment for 4 weeks. No significant change can be observed in the major organs, demonstrating great biocompatibility of HFTNPs (Figure S15).

4. CONCLUSIONS

In general, we have developed HFTNPs for enhanced MRI and inhibiting progression of plaques. HFTNPs with ultrasmall particle size can be effectively internalized by macrophages and induce further oxidant stress to specifically inhibit cell growth. In addition, the MRI contrast of plaques was tremendously enhanced via HFTNPs compared with that of clinical Gd-DOTA. In animal models, HFTNPs can specifically accumulate in atherosclerotic plaques and show higher SNR. Compared with free TA and HD-Fe³⁺, HFTNPs significantly prevented the progression of atherosclerotic plaques with no obvious side effects. To sum up, our research demonstrated the possibility and advantages of mild CDT in the diagnosis and treatment of atherosclerosis. HFTNPs have a tremendous potential as safe and effective diagnostic and therapeutic reagents for targeting chronic inflammation.

■ ASSOCIATED CONTENT

SI Supporting Information

The Supporting Information is available free of charge at <https://pubs.acs.org/doi/10.1021/acsami.1c09480>.

¹H NMR spectrum of HD; the absorption spectrum of HD-Fe³⁺ and HD-Fe³⁺-TA complex; T₁-weighted images and MR properties of Gd-DOTA; CLSM images and flow cytometry results of CD44 expression; detection of H₂O₂ in macrophages; the effect of HFTNPs against foam cells; biodistribution of HD-Fe³⁺ and HD-Fe³⁺-TA; lesion areas ratio of whole aorta; Prussian blue staining

and histological studies of major organs of ApoE^{-/-} mice (PDF)

■ AUTHOR INFORMATION

Corresponding Authors

Biao Xu – Department of Cardiology, Affiliated Nanjing Drum Tower Hospital of Nanjing University Medical School, Nanjing 210008, China; State Key Laboratory of Pharmaceutical Biotechnology, Nanjing University, Nanjing, Jiangsu 210023, China; Email: xubiao62@nju.edu.cn

Bing Zhang – Department of Radiology, Affiliated Nanjing Drum Tower Hospital of Nanjing University Medical School, Nanjing 210008, China; Institute of Brain Science, Nanjing University, Nanjing, Jiangsu 210008, China; orcid.org/0000-0001-7592-1195; Email: zhangbing_nanjing@nju.edu.cn

Authors

Dan Mu – Department of Radiology, Affiliated Nanjing Drum Tower Hospital of Nanjing University Medical School, Nanjing 210008, China

Wenshen Wang – National Lab for Physical Sciences at the Microscale and the Centers for Biomedical Engineering, University of Science and Technology of China, Hefei 230027, China

Jianhui Li – Department of Cardiology, Affiliated Nanjing Drum Tower Hospital of Nanjing University Medical School, Nanjing 210008, China

Pin Lv – Department of Radiology, Affiliated Nanjing Drum Tower Hospital of Nanjing University Medical School, Nanjing 210008, China

Renyuan Liu – Department of Radiology, Affiliated Nanjing Drum Tower Hospital of Nanjing University Medical School, Nanjing 210008, China

Ying Tan – Department of Cardiology, Affiliated Nanjing Drum Tower Hospital of Nanjing University Medical School, Nanjing 210008, China

Chongxia Zhong – Department of Cardiology, Affiliated Nanjing Drum Tower Hospital of Nanjing University Medical School, Nanjing 210008, China

Yu Qi – Department of Cardiology, Affiliated Nanjing Drum Tower Hospital of Nanjing University Medical School, Nanjing 210008, China

Xuan Sun – Department of Cardiology, Affiliated Nanjing Drum Tower Hospital of Nanjing University Medical School, Nanjing 210008, China

Yihai Liu – Department of Cardiology, Nanjing Drum Tower Hospital, Clinical College of Nanjing Medical University, Nanjing 210008, China

Song Shen – Department of Cardiology, Nanjing Drum Tower Hospital, Medical School of Nanjing University, Nanjing 210008, China

Yuyu Li – Department of Cardiology, Affiliated Nanjing Drum Tower Hospital of Nanjing University Medical School, Nanjing 210008, China

Complete contact information is available at:
<https://pubs.acs.org/doi/10.1021/acsami.1c09480>

Notes

The authors declare no competing financial interest.

ACKNOWLEDGMENTS

This work was supported by the National Natural Science Foundation of China (82070366; 81720108022, B.Z.; 81601539, D.M.); the Fundamental Research Funds for the Central Universities, Nanjing University (2020-021414380462); the key project of Jiangsu Commission of Health (K2019025); the social development project of science and technology project in Jiangsu Province (BE2017707); key medical talents of the Jiangsu Province, the "13th Five-Year" health promotion project of the Jiangsu Province (ZDRCA2016064); Jiangsu Provincial Key Medical Discipline (Laboratory) (ZDXKA2016020); the project of the sixth peak of talented people (WSN-138); the Nanjing Medical Science and technique Development Foundation (ZKX19018; QRX17057); China Postdoctoral Science Foundation (2019 M661804); and Jiangsu Province postdoctoral Science Foundation (2019 k060).

REFERENCES

- (1) Saigusa, R.; Winkels, H.; Ley, K. T Cell Subsets and Functions in Atherosclerosis. *Nat. Rev. Cardiol.* **2020**, *17*, 387–401.
- (2) Tabas, I.; Bornfeldt, K. E. Intracellular and Intercellular Aspects of Macrophage Immunometabolism in Atherosclerosis. *Circ. Res.* **2020**, *126*, 1209–1227.
- (3) Yin, L.; Peng, C.; Tang, Y.; Yuan, Y.; Liu, J.; Xiang, T.; Liu, F.; Zhou, X.; Li, X. Biomimetic Oral Targeted Delivery of Bindarit for Immunotherapy of Atherosclerosis. *Biomater. Sci.* **2020**, *8*, 3640–3648.
- (4) Mahjoubin-tehran, M.; Kovanen, P. T.; Xu, S.; Jamialahmadi, T.; Sahebkar, A. Pharmacology & Therapeutics Cyclodextrins: Potential Therapeutics against Atherosclerosis. *Pharmacol. Ther.* **2020**, *214*, No. 107620.
- (5) Dai, T.; He, W.; Yao, C.; Ma, X.; Ren, W.; Mai, Y.; Wu, A. *Biomater. Sci.* **2020**, *8*, 3784–3799.
- (6) Darwitan, A.; Wong, Y. S.; Nguyen, L. T. H.; Czarny, B.; Vincent, A.; Nedumaran, A. M.; Tan, Y. F.; Muktabar, A.; Tang, J. K.; Ng, K. W.; Venkatraman, S. Liposomal Nanotherapy for Treatment of Atherosclerosis. *Adv. Healthcare Mater.* **2020**, *9*, 1–11.
- (7) Stojanović, S. D.; Fiedler, J.; Bauersachs, J.; Thum, T.; Sedding, D. G. Senescence-Induced Inflammation: An Important Player and Key Therapeutic Target in Atherosclerosis. *Eur. Heart J.* **2020**, *41*, 2983–2996.
- (8) Lian, Z.; Perrard, X. Y. D.; Peng, X.; Raya, J. L.; Hernandez, A. A.; Johnson, C. G.; Lagor, W. R.; Pownall, H. J.; Hoogeveen, R. C.; Simon, S. I.; Sacks, F. M.; Ballantyne, C. M.; Wu, H. Replacing Saturated Fat With Unsaturated Fat in Western Diet Reduces Foamy Monocytes and Atherosclerosis in Male Ldlr^{-/-} Mice. *Arterioscler., Thromb., Vasc. Biol.* **2020**, *40*, 72–85.
- (9) Moreno-Franco, B.; Pérez-Esteban, A.; Civeira, F.; Guallar-Castillón, P.; Casasnovas, J. A.; Mateo-Gállego, R.; Jarauta, E.; Malo, S.; Laclaustra, M. Association between Alcohol Consumption and Subclinical Femoral Atherosclerosis in Smoking and Non-Smoking Men: The AWHs Study. *Addiction* **2020**, *115*, 1754–1761.
- (10) Gallego-Colon, E.; Daum, A.; Yosefy, C. Statins and PCSK9 Inhibitors: A New Lipid-Lowering Therapy. *Eur. J. Pharmacol.* **2020**, *878*, No. 173114.
- (11) Kouhpeikar, H.; Delbari, Z.; Sathyapalan, T.; Simental-Mendia, L. E.; Jamialahmadi, T.; Sahebkar, A. The Effect of Statins through Mast Cells in the Pathophysiology of Atherosclerosis: A Review. *Curr. Atheroscler. Rep.* **2020**, *22*, 19.
- (12) Alaarg, A.; Senders, M. L.; Varela-Moreira, A.; Pérez-Medina, C.; Zhao, Y.; Tang, J.; Fay, F.; Reiner, T.; Fayad, Z. A.; Hennink, W. E.; Metselaar, J. M.; Mulder, W. J. M.; Storm, G. A Systematic Comparison of Clinically Viable Nanomedicines Targeting HMG-CoA Reductase in Inflammatory Atherosclerosis. *J. Controlled Release* **2017**, *262*, 47–57.
- (13) Budoff, M. J.; Muhlestein, J. B.; Bhatt, D. L.; Le Pa, V. T.; May, H. T.; Shaikh, K.; Shekar, C.; Kinninger, A.; Lakshmanan, S.; Roy, S. K.; Tayek, J.; Nelson, J. R. *Cardiovasc. Res.* **2020**, *117*, 1–8. OUP Accepted Manuscript
- (14) Bejarano, J.; Navarro-Marquez, M.; Morales-Zavala, F.; Morales, J. O.; Garcia-Carvajal, I.; Araya-Fuentes, E.; Flores, Y.; Verdejo, H. E.; Castro, P. F.; Lavandero, S.; Kogan, M. J. Nanoparticles for Diagnosis and Therapy of Atherosclerosis and Myocardial Infarction: Evolution toward Prospective Theranostic Approaches. *Theranostics* **2018**, *8*, 4710–4732.
- (15) Yu, S.; Li, M.; Jing, S.; Dong, X.; Meng, M. Application of a Mechanically Responsive, Inflammatory Macrophage-Targeted Dual-Sensitive Hydrogel Drug Carrier for Atherosclerosis. *Colloids Surf., B* **2019**, *186*, No. 110718.
- (16) Maruf, A.; Wang, Y.; Yin, T.; Huang, J.; Wang, N.; Durkan, C.; Tan, Y.; Wu, W.; Wang, G. Atherosclerosis Treatment with Stimuli-Responsive Nanoagents: Recent Advances and Future Perspectives. *Adv. Healthcare Mater.* **2019**, *8*, 1–28.
- (17) Zia, A.; Wu, Y.; Nguyen, T.; Wang, X.; Peter, K.; Ta, H. T. The Choice of Targets and Ligands for Site-Specific Delivery of Nanomedicine to Atherosclerosis. *Cardiovasc. Res.* **2020**, 1–14.
- (18) Wijaya, A.; Maruf, A.; Wu, W.; Wang, G. Recent Advances in Micro- and Nano-Bubbles for Atherosclerosis Applications. *Biomater. Sci.* **2020**, *8*, 4920–4939.
- (19) Peters, E. B.; Kibbe, M. R. Nanomaterials to Resolve Atherosclerosis. *ACS Biomater. Sci. Eng.* **2020**, *6*, 3693–3712.
- (20) Flores, A. M.; Hosseini-Nassab, N.; Jarr, K. U.; Ye, J.; Zhu, X.; Wirka, R.; Koh, A. L.; Tsantilas, P.; Wang, Y.; Nanda, V.; Kojima, Y.; Zeng, Y.; Lotfi, M.; Sinclair, R.; Weissman, I. L.; Ingelsson, E.; Smith, B. R.; Leeper, N. Pro-Efferocytic Nanoparticles Are Specifically Taken up by Lesional Macrophages and Prevent Atherosclerosis. *Nat. Nanotechnol.* **2020**, *15*, 154–161.
- (21) Banik, B.; Surnar, B.; Askins, B. W.; Banerjee, M.; Dhar, S. Dual-Targeted Synthetic Nanoparticles for Cardiovascular Diseases. *ACS Appl. Mater. Interfaces* **2020**, *12*, 6852–6862.
- (22) Kim, M.; Sahu, A.; Hwang, Y.; Kim, G. B.; Nam, G. H.; Kim, I. S.; Chan Kwon, I.; Tae, G. Targeted Delivery of Anti-Inflammatory Cytokine by Nanocarrier Reduces Atherosclerosis in Apo E^{-/-} Mice. *Biomaterials* **2020**, *226*, No. 119550.
- (23) Gao, C.; Huang, Q.; Liu, C.; Kwong, C. H. T.; Yue, L.; Wan, J. B.; Lee, S. M. Y.; Wang, R. Treatment of Atherosclerosis by Macrophage-Biomimetic Nanoparticles via Targeted Pharmacotherapy and Sequestration of Proinflammatory Cytokines. *Nat. Commun.* **2020**, *11*, 2622.
- (24) Tang, J.; Lobatto, M. E.; Hassing, L.; Van Der Staay, S.; Van Rijs, S. M.; Calcagno, C.; Braza, M. S.; Baxter, S.; Fay, F.; Sanchez-Gaytan, B. L.; Duivenvoorden, R.; Sager, H. B.; Astudillo, Y. M.; Leong, W.; Ramachandran, S.; Storm, G.; Perez-Medina, C.; Reiner, T.; Cormode, D. P.; Strijkers, G. J.; Stroes, E. S. G.; Swirski, F. K.; Nahrendorf, M.; Fisher, E. A.; Fayad, Z. A.; Mulder, W. J. M. Inhibiting Macrophage Proliferation Suppresses Atherosclerotic Plaque Inflammation. *Sci. Adv.* **2015**, *1*, No. e1400223.
- (25) Lin, L. S.; Song, J.; Song, L.; Ke, K.; Liu, Y.; Zhou, Z.; Shen, Z.; Li, J.; Yang, Z.; Tang, W.; Niu, G.; Yang, H. H.; Chen, X. Simultaneous Fenton-like Ion Delivery and Glutathione Depletion by MnO₂-Based Nanoagent to Enhance Chemodynamic Therapy. *Angew. Chem., Int. Ed.* **2018**, *57*, 4902–4906.
- (26) Wang, Y.; An, L.; Lin, J.; Tian, Q.; Yang, S. A Hollow Cu₉S₈ Theranostic Nanoplatfrom Based on a Combination of Increased Active Sites and Photothermal Performance in Enhanced Chemodynamic Therapy. *Chem. Eng. J.* **2020**, *385*, No. 123925.
- (27) Ren, Z.; Sun, S.; Sun, R.; Cui, G.; Hong, L.; Rao, B.; Li, A.; Yu, Z.; Kan, Q.; Mao, Z. A Metal–Polyphenol-Coordinated Nanomedicine for Synergistic Cascade Cancer Chemotherapy and Chemodynamic Therapy. *Adv. Mater.* **2020**, *32*, No. 1906024.
- (28) Fu, S.; Yang, R.; Zhang, L.; Liu, W.; Du, G.; Cao, Y.; Xu, Z.; Cui, H.; Kang, Y.; Xue, P. Biomimetic CoO@AuPt Nanozyme Responsive to Multiple Tumor Microenvironmental Clues for

Augmenting Chemodynamic Therapy. *Biomaterials* **2020**, 257, No. 120279.

(29) Zhang, C.; Bu, W.; Ni, D.; Zhang, S.; Li, Q.; Yao, Z.; Zhang, J.; Yao, H.; Wang, Z.; Shi, J. Synthesis of Iron Nanometallic Glasses and Their Application in Cancer Therapy by a Localized Fenton Reaction. *Angew. Chem.* **2016**, 128, 2141–2146.

(30) Wang, M.; Chang, M.; Chen, Q.; Wang, D.; Li, C.; Hou, Z.; Lin, J.; Jin, D.; Xing, B. Au₂Pt-PEG-Ce6 Nanoformulation with Dual Nanozyme Activities for Synergistic Chemodynamic Therapy / Phototherapy. *Biomaterials* **2020**, 252, No. 120093.

(31) Tang, Z.; Liu, Y.; He, M.; Bu, W. Chemodynamic Therapy : Tumour Microenvironment- Mediated Fenton and Fenton-like Reactions. *Angew. Chem., Int. Ed. Engl.* **2019**, 58, 946–956.

(32) Miao, Y.; Xie, F.; Cen, J.; Zhou, F.; Tao, X.; Luo, J.; Han, G.; Kong, X.; Yang, X.; Sun, J.; Ling, J. Fe³⁺@polyDOPA-b-Polysarcosine, a T1-Weighted MRI Contrast Agent via Controlled NTA Polymerization. *ACS Macro Lett.* **2018**, 7, 693–698.

(33) Xin, K.; Li, M.; Lu, D.; Meng, X.; Deng, J.; Kong, D.; Ding, D.; Wang, Z.; Zhao, Y. Bioinspired Coordination Micelles Integrating High Stability, Triggered Cargo Release, and Magnetic Resonance Imaging. *ACS Appl. Mater. Interfaces* **2017**, 9, 80–91.

(34) Guo, J.; Ping, Y.; Ejima, H.; Alt, K.; Meissner, M.; Richardson, J. J.; Yan, Y.; Peter, K.; Von Elverfeldt, D.; Hagemeyer, C. E.; Caruso, F. Engineering Multifunctional Capsules through the Assembly of Metal-Phenolic Networks. *Angew. Chem., Int. Ed.* **2014**, 53, 5546–5551.

(35) He, W.; Kapate, N.; Shields, C. W.; Mitragotri, S. Drug Delivery to Macrophages: A Review of Targeting Drugs and Drug Carriers to Macrophages for Inflammatory Diseases. *Adv. Drug Delivery Rev.* **2019**, 165, 15–40.

(36) Lu, C.; Xiao, Y.; Liu, Y.; Sun, F.; Qiu, Y.; Mu, H.; Duan, J. Hyaluronic Acid-Based Levofloxacin Nanomicelles for Nitric Oxide-Triggered Drug Delivery to Treat Bacterial Infections. *Carbohydr. Polym.* **2020**, 229, No. 115479.

(37) Beldman, T. J.; Senders, M. L.; Alaarg, A.; Pérez-Medina, C.; Tang, J.; Zhao, Y.; Fay, F.; Deichmüller, J.; Born, B.; Desclos, E.; Wel, N.; Hoebe, R. A.; Kohen, F.; Kartvelishvili, E.; Neeman, M.; Reiner, T.; Calcagno, C.; Fayad, Z. A.; Winther, M. P. J.; Lutgens, E.; Mulder, W. J. M.; Kluza, E. Hyaluronan Nanoparticles Selectively Target Plaque-Associated Macrophages and Improve Plaque Stability in Atherosclerosis. *ACS Nano* **2017**, 11, 5785–5799.

(38) Zheng, D. W.; Lei, Q.; Zhu, J. Y.; Fan, J. X.; Li, C. X.; Li, C.; Xu, Z.; Cheng, S. X.; Zhang, X. Z. Switching Apoptosis to Ferroptosis: Metal-Organic Network for High-Efficiency Anticancer Therapy. *Nano Lett.* **2017**, 17, 284–291.

(39) Zhang, L.; Wan, S. S.; Li, C. X.; Xu, L.; Cheng, H.; Zhang, X. Z. An Adenosine Triphosphate-Responsive Autocatalytic Fenton Nanoparticle for Tumor Ablation with Self-Supplied H₂O₂ and Acceleration of Fe(III)/Fe(II) Conversion. *Nano Lett.* **2018**, 18, 7609–7618.

(40) Tang, C.; Amin, D.; Messersmith, P. B.; Anthony, J. E.; Prud'homme, R. K. Polymer Directed Self-Assembly of PH-Responsive Antioxidant Nanoparticles. *Langmuir* **2015**, 31, 3612–3620.

(41) Guo, Y.; Jia, H. R.; Zhang, X.; Zhang, X.; Sun, Q.; Wang, S. Z.; Zhao, J.; Wu, F. G. A Glucose/Oxygen-Exhausting Nanoreactor for Starvation- and Hypoxia-Activated Sustainable and Cascade Chemo-Chemodynamic Therapy. *Small* **2020**, 16, 1–9.

(42) Ju, Y.; Cui, J.; Müllner, M.; Suma, T.; Hu, M.; Caruso, F. Engineering Low-Fouling and PH-Degradable Capsules through the Assembly of Metal-Phenolic Networks. *Biomacromolecules* **2015**, 16, 807–814.

(43) Holten-Andersen, N.; Harrington, M. J.; Birkedal, H.; Lee, B. P.; Messersmith, P. B.; Lee, K. Y. C.; Waite, J. H. PH-Induced Metal-Ligand Cross-Links Inspired by Mussel Yield Self-Healing Polymer Networks with near-Covalent Elastic Moduli. *Proc. Natl. Acad. Sci. USA* **2011**, 108, 2651–2655.

(44) Ejima, H.; Richardson, J. J.; Liang, K.; Best, J. P.; Van Koeveerden, M. P.; Such, G. K.; Cui, J.; Caruso, F. One-Step Assembly

of Coordination Complexes for Versatile Film and Particle Engineering. *Science* **2013**, 341, 154–157.

(45) Yang, B.; Liu, Q.; Yao, X.; Zhang, D.; Dai, Z.; Cui, P.; Zhang, G.; Zheng, X.; Yu, D. FePt@MnO-Based Nanotheranostic Platform with Acidity-Triggered Dual-Ions Release for Enhanced MR Imaging-Guided Ferroptosis Chemodynamic Therapy. *ACS Appl. Mater. Interfaces* **2019**, 11, 38395–38404.

(46) Zhang, Y.; Wan, Y.; Liao, Y.; Hu, Y.; Jiang, T.; He, T.; Bi, W.; Lin, J.; Gong, P.; Tang, L.; Huang, P. Janus γ -Fe₂O₃/SiO₂-Based Nanotheranostics for Dual-Modal Imaging and Enhanced Synergistic Cancer Starvation/Chemodynamic Therapy. *Sci. Bull.* **2020**, 65, 564–572.